ADVANCED MATERIALS
www.advmat.de

The Fundamental Mechanism Behind Colossal Permittivity in Oxides

*Ned T. Taylor, Francis H. Davies, Shane G. Davies, Conor J. Price, and Steven P. Hepplestone**

Colossal permittivity materials exhibit extreme polarization in an applied electric field, providing applications in electronics and energy transmission. Understanding the atomic-scale mechanism behind colossal permittivity remains a challenging task and is key to optimizing materials with this property. The fundamental mechanism of colossal permittivity is reported and, using $CaCu_3Ti_4O_{12}$ as an example, it is attributed to the formation of an unusual metallic interface between the grain and grain boundary materials ($CaCu_3Ti_4O_{12}$ and Cu_xO (x = 1, 2), respectively), not created by oxygen vacancies as is normally the case in oxide materials. This metallic layer around the grain forms confined shells of charge that pool on one side when under an applied field, which results in colossal permittivity. A route towards enhancing colossal permittivity is explained by means of manipulating the interface properties, as well as altering sample geometries. A methodology to artificially engineer colossal permittivity metamaterials is also shown.

Colossal permittivity materials show values of relative permittivity, ε_r, typically greater than 10^3 and exhibit extreme polarization in an applied electric field. Given such high values for the permittivity, such materials offer new possibilities in sensing, electronic capacitors, and high power density energy storage.[1–3] The latter pairs have a vital potential role throughout the globe in electricity transmission across power grids. Colossal permittivity has been attributed to an effect known as the internal barrier layer capacitance (IBLC).[4–6] This phenomenon arises at the boundary between the individual grains that naturally form during crystal growth (the grain boundary). IBLC is often characterized experimentally by the Maxwell–Wagner effect,[7] but the microscopic origin behind this has not yet been determined or artificially engineered. Initial explanations for the mechanism behind colossal permittivity focused on Schottky-type effects.[4,8,9] However, these descriptions cannot simultaneously account for high loss factors, low breakdown voltages,[10] low resistance over grain boundaries,[11] nor how colossal permittivity scales with system size.[4,12–17] Colossal permittivity ranges by orders of magnitude in different materials,[18] but also in samples of the same stoichiometry.[19] This means there is an intrinsic effect in these materials which is responsible for IBLC. These conflicting accounts present some key issues with the description of the origin of IBLC.

It is apparent that the mechanism behind IBLC occurs between crystal grains, which are often identified as semiconducting,[5,20] while the material between the grains is shown to be insulating. To fully understand colossal permittivity it is necessary to understand the behavior of colossal permittivity in its archetype, $CaCu_3Ti_4O_{12}$ (CCTO). In CCTO, the IBLC mechanism is shown to occur at the grain boundary region.

In this paper, we apply first-principles density functional theory (DFT) and analytical continuum models in order to investigate colossal permittivity in CCTO, the archetype of this field, in order to understand the origins of this phenomenon. We identify the fundamental mechanism, at the atomic level, for colossal permittivity. Using CCTO as an example, we show that the grain boundary's structure results in the formation of an unusual metallic interface. To do this, we explore the phase space of the system and show that the grain boundary is an interface between CCTO and an oxide of copper, Cu_xO. It is the formation of this, unlike in other oxide interfaces, that creates the metallic interface, rather than oxygen vacancies. This metallic layer creates a shell of charge, trapped between two insulating regions, that is capable of facilitating extremely high charge polarization across the material. Our results are shown in the archetype of colossal permittivity, $CaCu_3Ti_4O_{12}$, with it providing a description for all materials that exhibit internal barrier layer capacitance. Current colossal permittivity materials can now be fully optimized based on the new mechanism described here, which also provides a route to artificially engineering colossal permittivity metamaterials.

Previous studies have investigated the role of copper migration in colossal permittivity.[21–23] In samples of CCTO, copper is generally found to migrate from the grain to the grain boundary region, where it likely forms a phase of copper oxide. This copper oxide has been attributed to the appearance of colossal permittivity, with the permittivity strongly depending on the properties, such as the resistivity, of this region. By modeling slabs of CCTO, we are

N. T. Taylor, F. H. Davies, S. G. Davies, C. J. Price, Dr. S. P. Hepplestone
School of Physics and Astronomy
University of Exeter
Stocker Road, Exeter EX4 4QL, UK
E-mail: S.P.Hepplestone@exeter.ac.uk

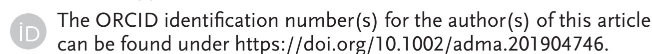
The ORCID identification number(s) for the author(s) of this article can be found under https://doi.org/10.1002/adma.201904746.

© 2019 The Authors. Published by WILEY-VCH Verlag GmbH & Co. KGaA, Weinheim. This is an open access article under the terms of the Creative Commons Attribution License, which permits use, distribution and reproduction in any medium, provided the original work is properly cited.

DOI: 10.1002/adma.201904746

able to find this copper migration. We find that copper closer to the surface becomes increasingly energetically favorable to form vacancies in the CCTO, where it can then form copper oxide. By analyzing the energetics of the various phases of Cu_xO we show that it is of the form of either CuO ($x = 1$) or Cu_2O ($x = 2$), with the stoichiometry depending strongly on the growth techniques, such as the relative concentration of oxygen present (see Figure S4 in the Supporting Information). This means that the grain boundary region is actually an interface between CCTO and Cu_xO.

Having explored the intergrain material, we now look to the potential surface terminations of CCTO. Here, we investigate two (001) termination planes (see the Supporting Information for a further discussion on the choice of surfaces), $CaCu_3O_4$- and TiO_2-terminated. While both are found to exhibit similar formation energies, the $CaCu_3O_4$ surface is found to be structurally unstable. Our results show that formation of copper and oxygen vacancies in the $CaCu_3O_4$-terminated surface is highly favorable, in agreement with the previously discussed copper migration. The creation of these vacancies depletes the top layer of copper and oxygen, which results in the TiO_2 layer below being exposed (and, thus, becoming the surface layer). This means that the only stable surface for the (001) plane of CCTO is the TiO_2-terminated surface. We are, therefore, left with an interface between TiO_2-terminated CCTO grains and the inter-grain Cu_xO material.

In order to examine the interface created between CCTO and Cu_xO at the atomic scale, we have developed an interface prediction tool that enables us to generate various interface structures and characterize them by their energetics obtained from first-principles calculations. Here, we present two interfaces likely to form, as shown in **Figure 1**. From these interfaces, we explore the electronic properties to obtain the atomic scale mechanism behind colossal permittivity.

Figure 1 shows the relaxed atomic geometry and electronic configurations of the two boundaries, CCTO/CuO and CCTO/Cu_2O. Figure 1a,d shows that the density of states associated with the interface layers are metallic. These states spread up to 3 Å from the interface and do not appear in the bulk, showing they are localized to the interface. Furthermore, far from the interface, the two bulk materials are insulating as their theoretical band gaps are recovered. If the copper oxide layer is less than 1 nm in thickness, then these metallic interface states merge, resulting in a continuous metallic region across the thin Cu_xO layer. An analysis of the charge distribution (see the Experimental Section) also supports this, indicating the atomic charges are only distorted below 3 Å from the interface into the copper oxide (Figure 1c,f). Also, regardless of whether the interface is oxygen-rich (Figure 1b) or copper-rich (Figure 1e) we find that both boundaries show this metallic behavior.

The metal layer has significant consequences for the material's dielectric characteristics. The shell of charge is localized around the grain, embedded in a Cu_xO shell (**Figure 2**), which prevents conduction. However, when an electric field is applied, this charge is drawn to one side of the grain. This effect creates a massive effective response in the polarization when an electric field is applied, akin to the Maxwell–Wagner effect commonly noted in the IBLC model. Thus, this is the fundamental mechanism, at the atomic scale, responsible for colossal permittivity. This metallic interface presented here leads to charge build-up at the interface in the grain boundary region, as shown in **Figure 3**a. This figure supports recent measurements for the current density[11] as higher charge density equates to higher current density. This argument also explains the scanning electron microscopy measurements[24] that show a higher charge density in the grain boundary region and how the permittivity of samples typically increases when the grain boundary resistance decreases.[11,25]

It is important to understand that, unlike most oxide interfaces, this metallic behavior is not created by oxygen vacancies, which is the normal mechanism for metallic interfaces in oxides[26] but actually due to the unusual structure of the interface. Here, we determine that the metallic region is caused by states unique to the interface created by the disorder in stoichiometry of the two materials at the interface, which results in one or more species being in excess. These interface states explain the freeze out in colossal permittivity, observed at very low temperatures[27] is clearly attributed to the narrowing of these states in the metallic interface.

To understand the nature of the metallic layer, we explore the composition of the states at the interface. From analysis of projected orbitals at the interface, as demonstrated by Figure 3b, we can attribute the states near the Fermi-level to a combination of oxygen-p orbitals and copper-d orbitals. These interface states have three characteristics which differentiate them from the bulk: i) the interface p orbitals are split, whereas they are degenerated in bulk CCTO; ii) the interface shows no significant d_{yz} contribution (<0.4%), contrary to bulk CCTO; iii) at the interface, the p_z and p_x orbitals are contribute more than the p_y ($p_z = 31.5\%$, $p_x = 30.1\%$, and $p_y = 10.1\%$ contributions), whereas, in bulk CuO, the p_y is dominant. This is different from oxygen vacancies where the missing atoms lead to a redistribution of charge on the nearby metal atoms. In addition, this characterization of the interface reveals that the metallic interface cannot be ascribed to a charge build up due to the band alignment, creating neither a Schottky barrier, nor a 2D electron gas. Both cases are characterized by a continuous distortion of the valence bands (or conduction bands), which result in a charge build-up at the interface between the two regions due to a potential well forming. Such a potential well would be demonstrated by the valence band maxima or conduction band minima showing high correspondence to their bulk counterparts, which is not the case here. Similarly, the conductive layers are not a result of conduction via π-bonds[28] as such bonding would show a regular, ordered pattern in the charge density across the interface. The topological plot, Figure 3b inset, demonstrates no features that can be attributed to such bond order and, thus, cannot be the cause of the metallic interfacial properties.

Hence, the previous discussion allows us to rule out the four most common mechanisms for metallic interface, i.e., i) oxygen vacancies, ii) charge build up due to band alignment, iii) conductive chains of π-bonds forming along the interface plane, and iv) by the energetic arguments discussed earlier, the formation of a Cu metal resulting in conduction. Thus, the metallic interface is caused by dopant or defect states localized to the interface formed by mismatched bonding between the two regions.

 © 2019 The Authors. Published by WILEY-VCH Verlag GmbH & Co. KGaA, Weinheim

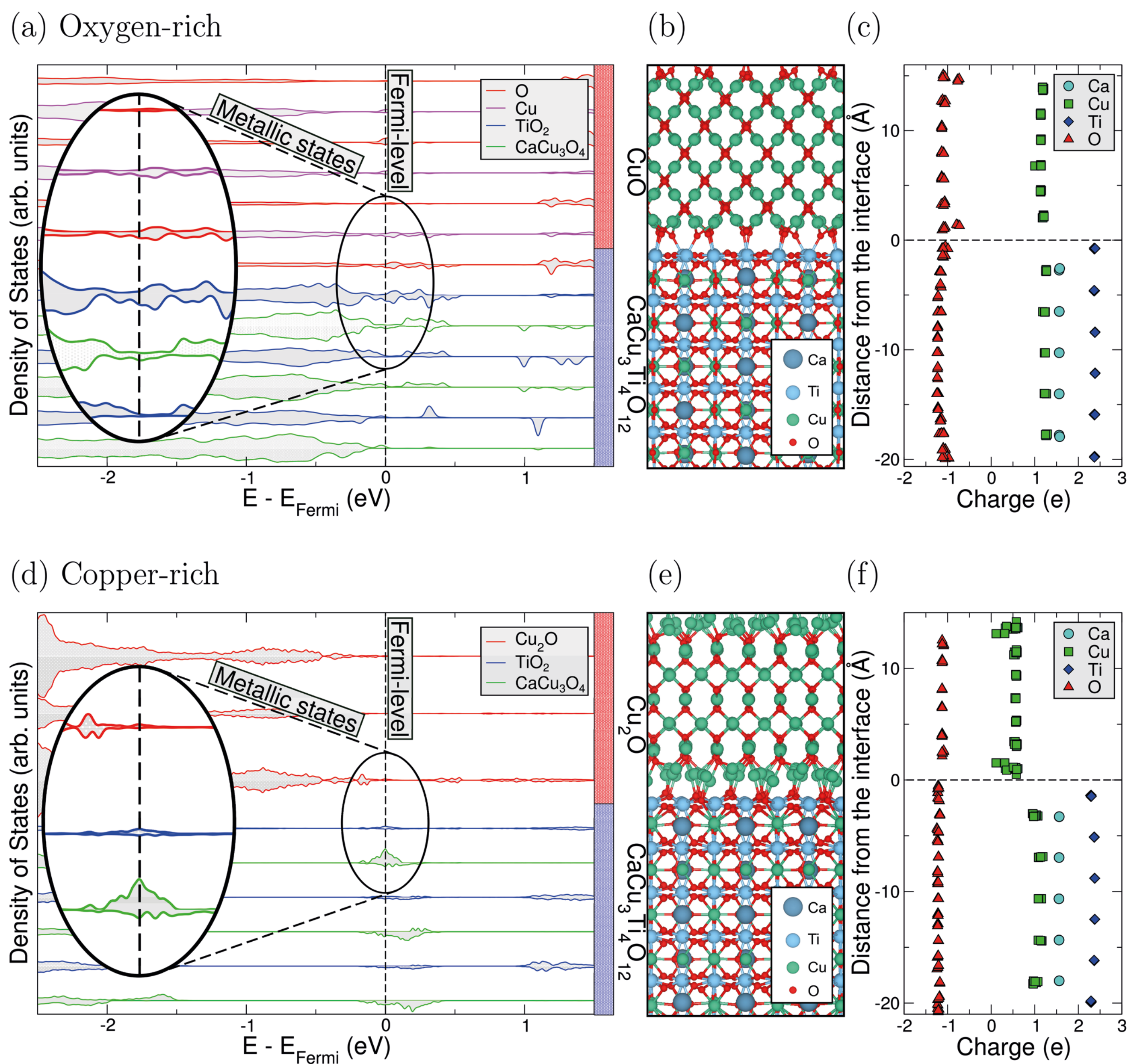

Figure 1. The electronic and geometric properties of a–c) CCTO/CuO and d–f) CCTO/Cu_2O interfaces. a,d) The layer-projected density of states of CCTO/CuO and CCTO/Cu_2O, respectively. The color legend denotes the atomic stoichiometry associated with each layer. The red/blue color bars denote the Cu_xO/CCTO regions. b,e) The structure of the CCTO/CuO and CCTO/Cu_2O interfaces, both viewed along the [110] direction of CCTO. The CuO region is terminated on an oxygen layer (oxygen-rich), and the Cu_2O region is terminated on a copper layer (copper-rich). c,f) The charge distribution analysis of the CCTO/CuO and CCTO/Cu_2O interfaces.

Thus far, we have shown that the oxygen vacancies are not responsible for the metallic interface, but it is important to understand how such vacancies would impact on the above discussion. The formation energy of individual oxygen vacancies is energetically more favorable near the interface, rather than in either the bulk CCTO or CuO regions, with a difference of 2.4 eV when compared to bulk CCTO (**Figure 4**). The introduction of these vacancies increases the number of states near the Fermi-level (Figure S5, Supporting Information), increasing the carrier concentration of the dilute metal, which, in turn, increases its conductivity. This increased conductivity means that we have a greater amount of charge to polarize, thus resulting in a higher colossal permittivity. This helps explain how the large variation in growth conditions can change the permittivity.[29] Critically, this result also explains the positive correlation between oxygen vacancy concentration and colossal permittivity.[30]

To illustrate how this atomic scale picture changes the macroscale, we have modeled the dielectric characteristics of the colossal permittivity material shown in Figure 2 as a series of

© 2019 The Authors. Published by WILEY-VCH Verlag GmbH & Co. KGaA, Weinheim

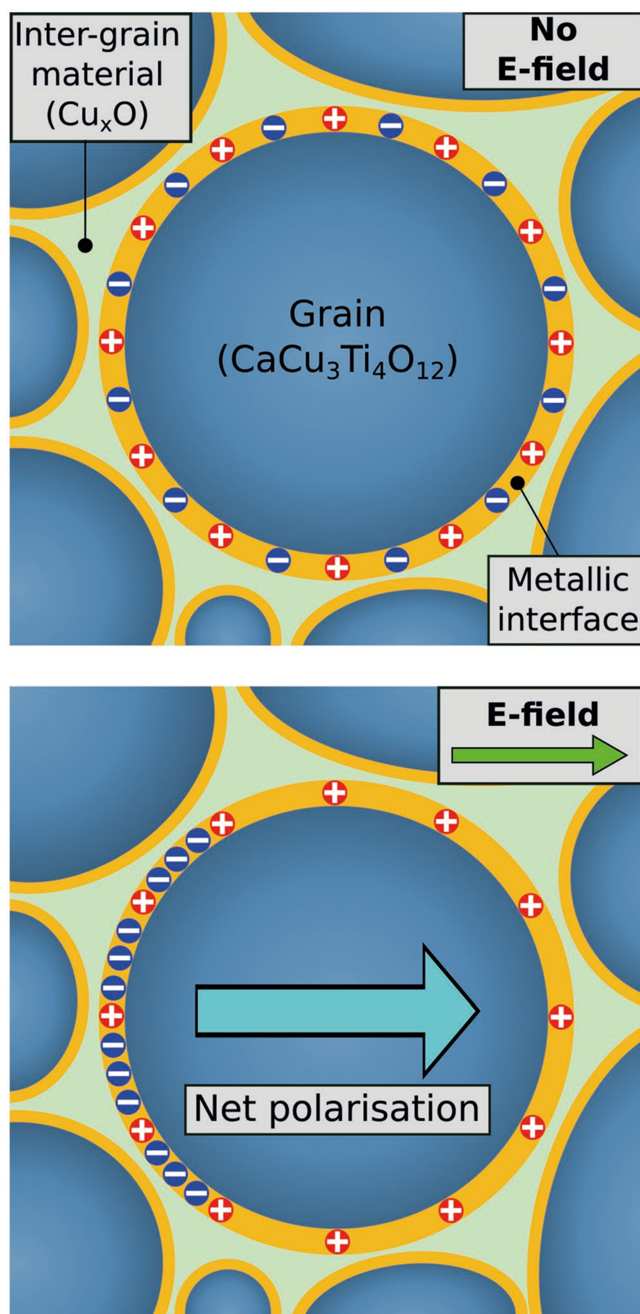

Figure 2. Schematic of the microscopic dielectric response of a colossal permittivity material. Diagram displaying charge confinement to the metallic interface between the nonmetallic regions of Cu_xO and $CaCu_3Ti_4O_{12}$ (the red and blue circles denote positive fixed ions and free-flowing electrons, respectively). In response to an electric field, these charges are seen to flow past the $CaCu_3Ti_4O_{12}$ but are still confined to this interface region due to the surrounding insulating Cu_xO intergrain material.

resistor-capacitor (RC) elements. This is analogous to applying impedance spectroscopy to such a system,[4,31,32] allowing for the measurement of permittivity (ε_r) and loss ($\tan(\delta)$), where loss is a description of the lifetime of the polarization of the material in the absence of an external field. Using our RC model, we show that an increase in grain size results in a larger permittivity (**Figure 5**), supporting existing experimental observations.[4,12–14] As a consequence of larger grain size, the volume of the surrounding dilute metal shell increases; as such, there is a greater amount of trapped charge that is able to be polarized under an applied electric field (Figure 2). Other adjustments to the system cannot account for the large changes in the dielectric response (Table S1, Supporting Information). A colossal permittivity metamaterial could be engineered by embedding metal shells inside of an insulating solid, mimicking the structure shown in Figure 2. This provides a route to producing artificial colossal permittivity materials. This mechanism offers new insight into the metallic behavior seen in a range of oxide interfaces, due to the origin being different from the majority. To investigate this phenomenon further, we propose applying a large magnetic field perpendicular to the a.c. electric field. This will result in a polarization component perpendicular to both fields.

In summary, we have employed first-principles density functional theory methods to investigate colossal permittivity. In doing so, we attribute the fundamental phenomenon behind this to an unusual metal interface forming in the grain boundary region. This metallic interface is unusual in that it is not created by oxygen vacancies, but due to the breakdown in stoichiometry at the interface. Due to the confined shells of charge created, an applied field moves the charge to one side of the grain, resulting in a massive polarization and thus colossal permittivity. This effect can be enhanced by either adding (or in reality increasing) the concentration of oxygen vacancies or by increasing the grain sizes. Our results provide a new understanding of oxide interfaces and colossal permittivity and provide a future method for how both could be manipulated and characterized.

Experimental Section

Density Functional Theory Calculations: First-principles calculations, within the framework of DFT, were performed using the Vienna Ab Initio Simulation Package (VASP).[33–35] These calculations obtained the structural and electronic properties of the systems outlined in this work. The generalized gradient approximation (GGA) Perdew–Burke–Ernzerhof (PBE)[36] functional using plane-waves and the projector-augmented-wave method[37] were used for structural relaxations. The valence electrons for each atomic species are considered as follows: $3s^23p^64s^2$ for Ca, $3d^{10}4s^1$ for Cu, $3p^63d^44s^2$ for Ti, and $2s^22p^4$ for O. k-point grids were selected and systems were compared using k-point densities equivalent to those used for analyzing the $CaCu_3Ti_4O_{12}$ (CCTO) 40-atom unit cell, with geometric relaxations and electronic calculations using $4\times4\times4$ and $7\times7\times7$ grids, respectively. All k-point grids were Γ-centred and generated using the Monkhorst–Pack scheme.[38] All systems are geometrically relaxed to within 0.01 eV Å^{-1}. To accurately describe the insulating properties of CCTO and Cu_xO, the Hubbard GGA+U model was applied. The range $U = 0$ to 10 eV was fully explored to confirm the results hold for all values. For the results presented, a $+U$ correction of +4 eV was used for the Cu in the $CaCu_3Ti_4O_{12}$ and Cu_2O, and $U = +7$ eV for the Cu in CuO. The experimental bulk bandgaps of CCTO, CuO and Cu_2O were reproduced, with values of 1.5 eV,[39] 1.2 eV,[40] and 2.17 eV,[41] respectively. The charge analysis of these systems was performed using the Bader technique.[42]

Atomic Geometry: To create the interfaces, the in house code ARTEMIS (Ab initio restructuring tool enabling the modelling of interface structures) was used, which generates interface structures and corresponding slabs of materials for atomic scale analysis. The CCTO

© 2019 The Authors. Published by WILEY-VCH Verlag GmbH & Co. KGaA, Weinheim

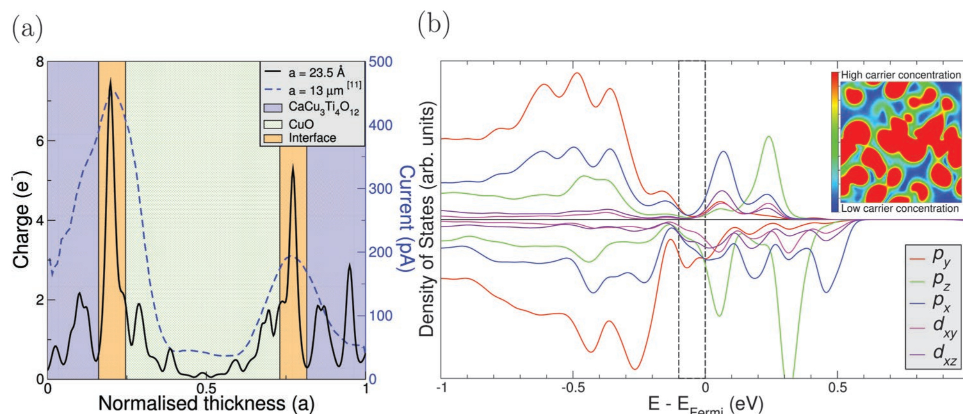

Figure 3. Properties of the metallic interface in the CCTO/CuO system. a) Dependence of the free charge (current) on location within the CCTO/CuO system, denoted by the black (blue) line. The black line denotes a 1D plot of the partial charge density ranging from −0.1 eV to the Fermi energy along the (001) direction. The blue line displays measurements of current at different points through a CCTO sample (data adapted from ref. [11]). The different regions of the sample are labeled. b) The orbital density of states associated with the interface states of the CCTO/CuO system shown in Figure 1b. The inset depicts a color map displaying a 2D cut of the partial charge for the structure taken through the [001] plane at the interface between the CCTO and CuO regions, with an energy range of −0.1 eV to the Fermi energy (energy range between the two dashed lines in the main figure). Red and blue denote greater and lesser charge, respectively.

and CuO slab thicknesses were increased until convergence of various electronic properties was reached. As such, CCTO regions of 2.5 unit cell thickness were used in the grain boundary systems. The same analysis was performed for CuO and Cu_2O. These comparisons allows for the consideration of CCTO/Cu_xO interfaces in general. The CCTO (001) surface was modeled at the interface as other planes bring further complications as they are generally found to be polar, with dangling bonds or nonstoichiometric surfaces, which can lead to instability of the surface. The properties of this surface are examined in the Supporting Information. Various Cu_xO phases and cleavage planes were considered in order to find surfaces matching with the (001) CCTO surface, with a strain tolerance of 6%. The Cu_xO strain tolerance for the $x = 1$ and $x = 2$ were 5.06 % and 1.31 %, respectively.

Interfaces formed of either termination of CCTO or choice of Cu_xO are found to show qualitatively similar results. Therefore, the CCTO/CuO structure was considered as the archetype interface. The interface system consists of 2.5 CCTO unit cells, terminated on TiO_2 planes, next to a 3 unit cell slab of monoclinic CuO that was orthorhombically strained. The choice of thicknesses was made in order to recover the respective bulk properties within the center of each region. In total, 10 unique interface structures composed of CCTO and Cu_xO were considered for this study. These unique interfaces consisted of a set of different orientations and terminations, with all displaying qualitatively similar results to those presented in Figure 1. The focus on the two interfaces presented in the article is due to other interfaces being energetically less favorable or involving substantial reconstruction of the Cu_xO (leading to amorphous Cu_xO).

Impedance Calculations: Impedance calculations[43–45] were modeled using a constant phase element approach.[46] This involved describing each component in the system as resistor–capacitor (RC) parallel elements. CCTO grains and Cu_xO grain boundaries were described as RC elements, while the metallic interface and electrodes were described as purely resistor elements. From this, a large network of grains, interfaces, and grain boundaries connected between two electrodes was obtained.

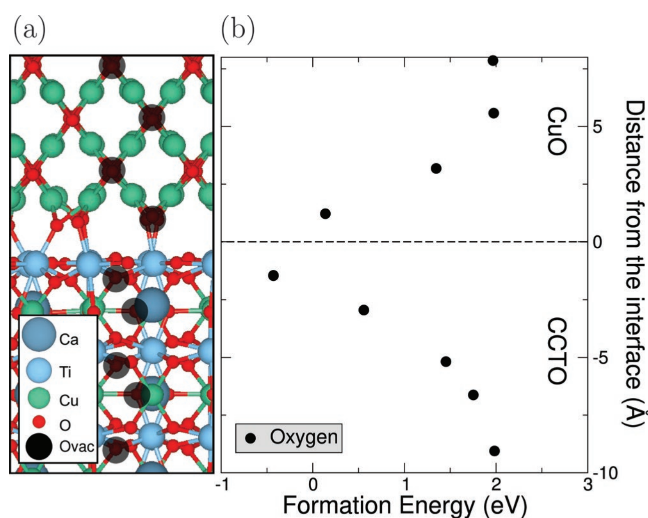

Figure 4. Oxygen vacancies near the CCTO/CuO interface. a) Simulated locations of individual oxygen vacancies in the CCTO/CuO interface system. b) The formation energy of the vacancies as a function of distance from the interface with individual locations depicted in (a).

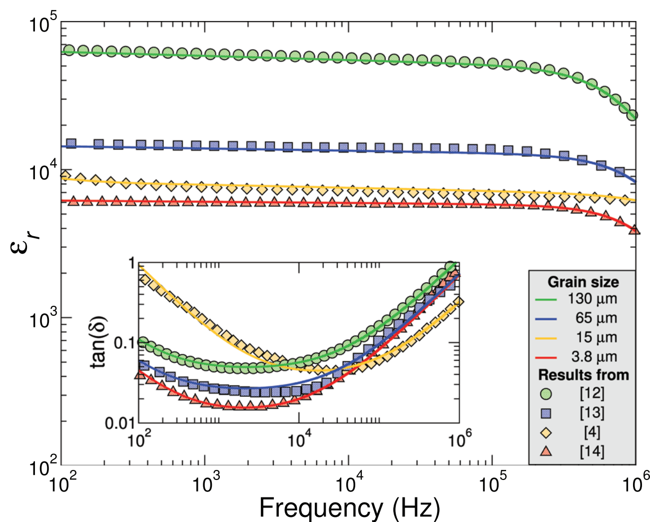

Figure 5. Dielectric response in colossal permittivity materials. Permittivity (ε_r) and dielectric loss ($\tan(\delta)$) plots of a resistor–capacitor circuit model and experimental data (experimental data adapted from refs. [4,12–14]).

© 2019 The Authors. Published by WILEY-VCH Verlag GmbH & Co. KGaA, Weinheim

Supporting Information

Supporting Information is available from the Wiley Online Library or from the author.

Acknowledgements

Via our membership of the UK's HEC Materials Chemistry Consortium, which is funded by EPSRC (EP/L000202, EP/R029431), this work used the ARCHER UK National Supercomputing Service (http://www.archer.ac.uk). Also, all of the authors acknowledge funding from the EPSRC (EP/L015331/1). S.P.H. thanks Deregallera for funding and useful discussions. Finally, the authors thank David Horsell, Eros Mariani, and Elizabeth L. Martin for their useful discussions. N.T.T. carried out the bulk of the calculations and modeling. F.H.D. carried out some supporting calculations. N.T.T., F.H.D., and S.P.H. developed ARTEMIS with structural testing by S.G.D. and C.J.P. All authors supported the analysis of the data. S.P.H. conceived and supervised the project.

Conflict of Interest

The authors declare no conflict of interest.

Keywords

calcium copper titanate, CCTO, colossal permittivity, copper, first-principles calculations, titanate

Received: July 24, 2019
Revised: September 19, 2019
Published online:

[1] R. K. Pandey, W. A. Stapleton, J. Tate, A. K. Bandyopadhyay, I. Sutanto, S. Sprissler, S. Lin, *AIP Adv.* **2013**, *3*, 062126.
[2] R. Löhnert, H. Bartsch, R. Schmidt, B. Capraro, J. Töpfer, *J. Am. Ceram. Soc.* **2015**, *98*, 141.
[3] M. A. Ponce, M. A. Ramirez, F. Schipani, E. Joanni, J. P. Tomba, M. S. Castro, *J. Eur. Ceram. Soc.* **2015**, *35*, 153.
[4] T. Adams, D. Sinclair, A. West, *Adv. Mater.* **2002**, *14*, 1321.
[5] D. C. Sinclair, T. B. Adams, F. D. Morrison, A. R. West, *Appl. Phys. Lett.* **2002**, *80*, 2153.
[6] P. Salame, R. Drai, O. Prakash, A. R. Kulkarni, *Ceram. Int.* **2014**, *40*, 4491.
[7] R. Sillars, *Inst. Electr. Eng.-Proc. Wirel. Sect. Inst.* **1937**, *12*, 139.
[8] I.-D. Kim, A. Rothschild, H. L. Tuller, *Appl. Phys. Lett.* **2006**, *88*, 072902/1.
[9] M. Li, Z. Shen, M. Nygren, A. Feteira, D. C. Sinclair, A. R. West, *J. Appl. Phys.* **2009**, *106*, 104106.
[10] C. Zhao, J. Wu, *ACS Appl. Mater. Interfaces* **2018**, *10*, 3680.
[11] M. S. Ivanov, F. Amaral, V. A. Khomchenko, J. A. Paixão, L. C. Costa, *RSC Adv.* **2017**, *7*, 40695.
[12] S. De Almeida-Didry, C. Autret, A. Lucas, C. Honstettre, F. Pacreau, F. Gervais, *J. Eur. Ceram. Soc.* **2014**, *34*, 3649.
[13] S. F. Shao, J. L. Zhang, P. Zheng, W. L. Zhong, C. L. Wang, *J. Appl. Phys.* **2006**, *99*, 084106.
[14] P. Thongbai, S. Pinitsoontorn, V. Amornkitbamrung, T. Yamwong, S. Maensiri, P. Chindaprasirt, *Int. J. Appl. Ceram. Technol.* **2013**, *10*, E77.
[15] T. Adams, D. Sinclair, A. West, *J. Am. Ceram. Soc.* **2006**, *89*, 3129.
[16] W. Li, O. Auciello, R. N. Premnath, B. Kabius, *Appl. Phys. Lett.* **2010**, *96*.
[17] P. Walke, R. Bouregba, A. Lefevre, G. Parat, F. Lallemand, F. Voiron, B. Mercey, U. Lüders, *J. Appl. Phys.* **2014**, *115*, 094103.
[18] J. Sun, R. Ahmed, G. J. Wang, S. T. Wang, J. Wang, S. A. Suhaib, Y. M. Xie, H. Bi, C. C. Wang, *J. Mater. Sci.* **2019**, *54*, 6323.
[19] T. T. Fang, L. T. Mei, H. F. Ho, *Acta Mater.* **2006**, *54*, 2867.
[20] G.-L. Li, Z. Yin, M.-S. Zhang, *Phys. Lett. A* **2005**, *344*, 238.
[21] T. Lebey, S. Guillemet, V. Bley, M. Boulos, B. Durand, *IEEE Electron.* **2005**, *55*, 1248.
[22] R. Schmidt, S. Pandey, P. Fiorenza, D. C. Sinclair, *Rsc Adv.* **2013**, *3*, 14580.
[23] W. X. Yuan, Z. Luo, C. Wang, *J. Alloys Compd.* **2013**, *562*, 1.
[24] D. Fu, H. Taniguchi, T. Taniyama, M. Itoh, S.-y. Koshihara, *Chem. Mater.* **2008**, *20*, 1694.
[25] K. Chen, G. L. Li, F. Gao, J. Liu, J. M. Liu, J. S. Zhu, *J. Appl. Phys.* **2007**, *101*, 074101.
[26] B. W. Veal, S. K. Kim, P. Zapol, H. Iddir, P. M. Baldo, J. A. Eastman, *Nat. Commun.* **2016**, *7*, 1.
[27] P. B. A. Fechine, A. F. L. Almeida, F. N. A. Freire, M. R. P. Santos, F. M. M. Pereira, R. Jimenez, J. Mendiola, A. S. B. Sombra, *Mater. Chem. Phys.* **2006**, *96*, 402.
[28] S. J. Jenkins, G. P. Srivastava, *Surf. Sci.* **1996**, *352–354*, 411.
[29] P. Mao, J. Wang, S. Liu, L. Zhang, Y. Zhao, L. He, *J. Alloys Compd.* **2019**, *778*, 625.
[30] F. Y. Liao, C. L. Chen, D. Y. Feng, M. Gao, L. B. Jin, Y. Lin, Y. Zhang, G. Yao, Y. D. Ji, *J. Mater. Chem. C* **2015**, *3*, 3438.
[31] T. T. Fang, C. P. Liu, *Chem. Mater.* **2005**, *17*, 5167.
[32] N. J. Kidner, N. H. Perry, T. O. Mason, E. J. Garboczi, *J. Am. Ceram. Soc.* **2008**, *91*, 1733.
[33] G. Kresse, J. Hafner, *Phys. Rev. B* **1993**, *47*, 558.
[34] G. Kresse, J. Furthmüller, *Phys. Rev. B* **1996**, *54*, 11169.
[35] G. Kresse, J. Furthmüller, *Comput. Mater. Sci.* **1996**, *6*, 15.
[36] J. P. Perdew, K. Burke, M. Ernzerhof, *Phys. Rev. Lett.* **1996**, *77*, 3865.
[37] G. Kresse, *Phys. Rev. B* **1999**, *59*, 1758.
[38] J. D. Pack, H. J. Monkhorst, *Phys. Rev. B* **1977**, *16*, 1748.
[39] H. Im, M. Iwataki, S. Yamazaki, T. Usui, S. Adachi, M. Tsunekawa, T. Watanabe, K. Takegahara, S. Kimurac, M. Matsunami, H. Sato, H. Namatame, M. Taniguchi, *Solid State Commun. J.* **2015**, *217*, 17.
[40] K. M. Shrestha, C. M. Sorensen, K. J. Klabunde, *Scan. Electron Microsc.* **2010**, *114*, 14368.
[41] B. K. Meyer, A. Polity, D. Reppin, M. Becker, P. Hering, P. J. Klar, T. Sander, C. Reindl, J. Benz, M. Eickhoff, C. Heiliger, M. Heinemann, J. Bläsing, A. Krost, S. Shokovets, C. Müller, C. Ronning, *Phys. Status Solidi Basic Res.* **2012**, *249*, 1487.
[42] R. F. W. Bader, *Chem. Rev.* **1991**, *91*, 893.
[43] I. M. Hodge, M. D. Ingram, A. R. West, *J. Electroanal. Chem.* **1976**, *74*, 125.
[44] J. T. S. Irvine, D. C. Sinclair, A. R. West, *Adv. Mater.* **1990**, *2*, 132.
[45] M. J. Pan, B. A. Bender, *J. Am. Ceram. Soc.* **2005**, *88*, 2611.
[46] J.-B. Jorcin, M. E. Orazem, N. Pébère, B. Tribollet, *Electrochim. Acta* **2006**, *51*, 1473.

© 2019 The Authors. Published by WILEY-VCH Verlag GmbH & Co. KGaA, Weinheim